Merging strut-based and minimal surface meta-biomaterials
Decoupling surface area from mechanical properties

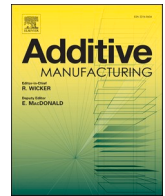Kolken, H. M.A.; Callens, S. J.P.; Leeflang, M. A.; Mirzaali, M. J.; Zadpoor, A. A.

Important note
To cite this publication, please use the final published version (if applicable).
Please check the document version above.

Merging strut-based and minimal surface meta-biomaterials: Decoupling surface area from mechanical properties

H.M.A. Kolken [*], S.J.P. Callens, M.A. Leeflang, M.J. Mirzaali, A.A. Zadpoor

Department of Biomechanical Engineering, Delft University of Technology, Delft, The Netherlands

A B S T R A C T

The rational design of bone-substituting biomaterials is relatively complex because they should meet a long list of requirements for optimal performance. Meta-biomaterials are micro-architected materials that hold great promise for meeting those requirements as they offer a unique combination of mechanical, mass-transport, and biological properties. There are, however, inherent couplings between the different types of properties of many such materials that make it impossible to simultaneously achieve all the design criteria. An example of such a coupling exists between the mechanical properties and the surface area. Strut-based, metallic meta-biomaterials are known to offer bone-mimicking mechanical properties, but they have limited surface area for cell adherence. Increasing the surface generally results in an undesirable increase in the mechanical properties that could lead to stress shielding. Here, we combine strut-based lattices with minimal surfaces to decouple these two properties. We added minimal surface patches to the designs of both auxetic and non-auxetic meta-biomaterials while minimizing their contribution to the mechanical properties of the resulting meta-biomaterials through the rational application of cuts or "slits". All designs were additively manufactured using selective laser melting and mechanically tested to obtain their *quasi-static* mechanical properties, including their Poisson's ratio, in two configurations. A finite element-based computational homogenization code was used to compute the elastic moduli and anisotropy of the structures. The results show that the minimal surface patches substantially increase the available surface area without significantly affecting the mechanical properties. Without the slits, the surfaces significantly affected the elastic modulus and deformation behavior of the meta-biomaterials. A similar strategy could be used to tune the biodegradation rate of biodegradable metals and the permeability of meta-biomaterials in general.

1. Introduction

The fundamental idea behind metamaterials is that their macroscale properties can be tuned through slight alterations in their microscale architecture. This geometry-property connection has been exploited to develop various metamaterials with unusual mechanical properties [1–3]. Bone tissue engineering is one of the disciplines that could benefit from these designer materials, since bone implants should meet a long list of requirements for optimal performance.

These requirements go far beyond simply solving the long-standing problem of stress-shielding, now that the world population is aging and the prevalence of osteoarthritis is rising, especially among younger patients [4–6]. Within the context of bone tissue engineering, these so-called meta-biomaterials are designed to meet the requirements regarding the mechanical, mass-transport and biological properties of an optimal bone substitute [1,2,7]. Targeting several properties at once introduces a certain level of complexity, since most properties are coupled through the geometry of the structure. One could for instance increase the mechanical properties of a meta-biomaterial by increasing its relative density, but this generally results in a lower porosity and a smaller pore size. These morphological features have been proven essential in promoting bone tissue regeneration and osseointegration, and should, therefore, stay within the experimentally defined limits [8].

While decoupling the aforementioned properties is challenging, it is not impossible. The advances in multi-material additive manufacturing have enabled the spatial distribution of multiple materials across one single volume. Every voxel of printed materials can now be programmed to exhibit different material properties than the next, owing to the different properties of the base materials used [9–11]. We recently proposed a new parametric design strategy to decouple the elastic

---

properties and permeability of triply periodic minimal surfaces (TPMS), through the allocation of hard, soft, and void phases [12]. To date, the above-mentioned multi-material additive manufacturing techniques have only been applied in combination with hard and soft polymers, which limits its application in (load bearing) bone substitutes.

Metals and their alloys are highly attractive materials for skeletal repair [13]. Stainless steels, cobalt-based alloys (*e.g.*, CoCrMo), and titanium (Ti) as well as its alloys (Ti-6Al-4V) have established themselves as biocompatible metallic biomaterials that offer superior mechanical strength and high degrees of corrosion resistance [13,14]. However, their bulk properties generally exceed those of the bony tissue, which may result in stress shielding and ultimately implant loosening [15,16]. Porous metallic bone scaffolds have, therefore, been introduced to reduce the amount of material and, thus, the mechanical properties. With the introduction of laser powder bed fusion techniques such as selective laser melting (SLM), it is now possible to manufacture these complex micro-architectures using metallic powder as feedstock. These rather complex 3D shapes often consist of strut-based arrays of unit cells, which gives them sufficient porosity to not only accommodate tissue integration, but to also decrease their mechanical properties to the level of the native bony tissue [17].

Strut-based meta-biomaterials, therefore, form a promising basis for bone tissue regeneration, but they do limit the amount of surface area available for cell adhesion. To increase the surface area, one could increase the strut thickness, but this would lead to substantially increased mechanical properties. In this study, we propose a new strategy to decouple the mechanical properties of metallic meta-biomaterials, including their Poisson's ratio, from the surface area available for cell adhesion. This approach combines strut-based lattices with extraordinary properties (*e.g.*, negative Poisson's ratio (NPR)) with minimal surfaces. Strut-based lattices and minimal surfaces have been widely studied within the context of bone tissue engineering [1–3,18], serving as templates for bone substitutes that could mimic the complex geometry of native bone tissue [19]. The properties of strut-based lattices can be tuned to recapitulate the mechanical characteristics of the host bone, while minimal surfaces are mechanically efficient and famed for their fascinating geometrical features. Here, we propose to add minimal surface patches to the designs of both auxetic and non-auxetic meta--biomaterials while minimizing their contribution to the effective mechanical properties of the meta-biomaterials through the rational introduction of cuts or 'slits'. Control groups are used to compare the properties of the resulting meta-biomaterials with those of strut-based lattices without the minimal surface patches and to geometrically similar designs without the rational application of the slits. All designs were additively manufactured and mechanically tested to measure the *quasi-static* mechanical properties. Digital image correlation (DIC) was used to measure the local displacements and hence, the Poisson's ratio. Finite element (FE) simulations were run to compute the effective elastic modulus and anisotropy of the structures.

2. Materials and methods

2.1. Design of auxetic and non-auxetic meta-biomaterials

In this work, we propose an approach to increase the surface area of several meta-biomaterials independently of their mechanical properties. This rational approach relies on adding surface patches to specific regions of strut-based lattices and adding cuts or 'slits' to the surfaces to limit their contribution to the overall mechanical properties. In principle, this procedure could be applied to any type of strut-based lattice structure. However, we have chosen for the widely studied hexagonal honeycomb (*i.e.*, non-auxetic) and its auxetic counterpart, the re-entrant hexagonal honeycomb [20,21]. This choice of unit cell allows us to readily vary the Poisson's ratio of the resulting meta-biomaterials and achieve both positive (PPR) and negative (NPR) values of the Poisson's ratio. The lattices were designed in Solidworks (Dassault Systèmes,

Vélizy-Villacoublay, France). The structures consisted of a $5 \times 5 \times 5$ unit cell array with a strut thickness of 400 µm. Previous work has shown that the aspect ratio (*a/b*) and structural angle (*θ*) of the unit cells both influence the mechanical properties of the structure as a whole (Fig. 1A-B) [1,20]. A constant aspect ratio of 1.5 and uniform cell width of 2.36 mm were chosen for both non-auxetic (C) and auxetic (A) lattices as well as a 115° and 65° structural angle (*θ*), respectively. The exact unit cell dimensions can be found in Table 1.

To decorate the lattices with surface patches, closed-loop 'wireframes' without self-intersections were identified in the unit cells to which the surfaces could be attached (Fig. 1). When considering the lattice as a mathematical graph, such closed wireframes correspond to cycles in the graph. In some cases, these closed wireframes could be planer polygons (*e.g.* the square face of the simple cubic lattice), but in general these wireframes are skew polygons [18]. To define a surface spanning a skew *n*-gon (with *n* representing the number of edges), the minimal surface spanning that *n*-gon was numerically computed using Surface Evolver [22]. For any given wireframe, the minimal surface is the surface of minimal area, and all minimal surfaces are characterized by a vanishing mean curvature and a negative (or zero) Gaussian curvature. The triangulated minimal surfaces obtained using Surface Evolver were converted to solid patches (*i.e.* were assigned a thickness) by offsetting the mesh vertices in their normal directions and closing off the resulting parallel meshes along their boundaries. This operation, which was performed using some of the functions of the Gibbon toolbox (*tesGroup*, *patchNormal*) in Matlab (version 2018b, Mathworks, Natick, MA, USA) [23], resulted in minimal surface patches with a thickness of 200 µm. The surface patches were exported in the STL file format and imported into Solidworks, to be assembled with the lattices (with surfaces and without the slits = WS) (Figs. 2B and F). For the designs with surfaces and slits (with slits = S), the surface patches were cut into several pieces, in such a way that each disconnected piece was only connected to one single strut, effectively disabling load transfer from one strut to another through the surface patches. A 175 µm diagonal cut was made and sides were cropped by 120 µm, resulting in two triangular surfaces patches (Figs. 2C and G). The assembled structures were combined and exported in the STL file format.

2.2. Additive manufacturing of metallic meta-biomaterials

The specimens were manufactured with SLM using an SLM125 machine (Realizer GmbH, Borchen, Germany). The machine was equipped with a 400 W Ytterbium fiber laser (IPG Photonics Corporation, Oxford, USA). Spherical, plasma-atomized Ti-6Al-4V ELI powder with a particle size of 10–45 µm (AP&C, Boisbriand, Canada) was used as the feedstock. During printing, the oxygen level in the build chamber was kept below 0.2% using an Argon flow. The substrate plate was kept constant at 100 °C.

A slicer program, RDesigner (Realizer GmbH, Borchen, Germany), was used to prepare the build. The specimens were rotated by 45° and 35° around the y- and x-axis, respectively, to create an internal self-supporting structure. On the build plates, 16 locations of 20 mm × 23 mm were defined on which one specimen could be built. The different design configurations were divided over the build plates to avoid mechanical or dimensional deviations caused by specimen location or inhomogeneous powder coating. A successful combination of the processing parameters was found through trial and error (Table 2), and ten specimens of each design were built. Since the lattices and the surface patches were combined in one file, they were also printed using a single laser scanning strategy.

2.3. Morphological characterization

The morphology of the six designs is primarily different in terms of the specific surface area and the permeability. The surface area was, therefore retrieved from the three-dimensional CAD files using the
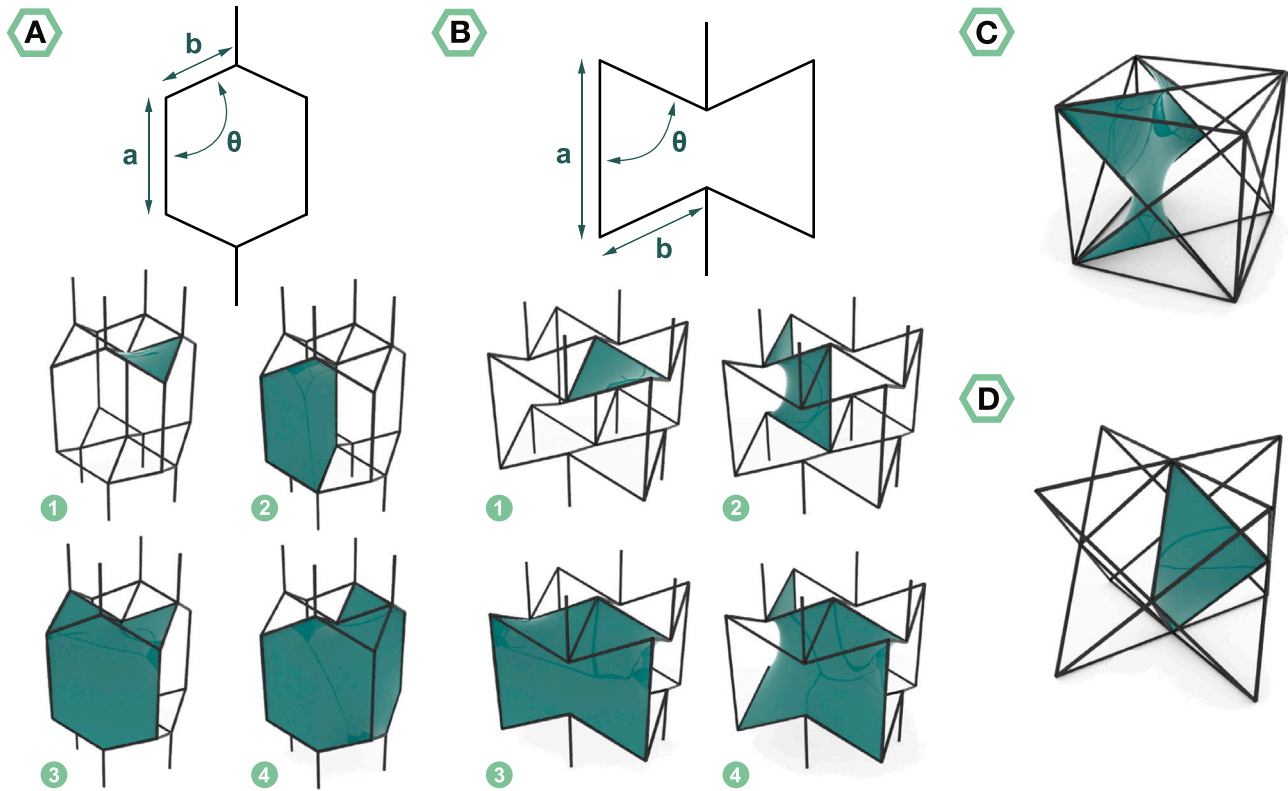
Fig. 1. 2D line drawing with design parameters *a*, *b*, and *θ* of the (A) hexagonal honeycomb and (B) re-entrant hexagonal honeycomb. A1–4 shows the design possibilities with the hexagonal honeycomb using 4-, 6-, 8-, and 10-gon minimal surface patches, respectively. B1–4 shows the design possibilities with the re-entrant hexagonal honeycomb using 4-, 6-, 8-, and 10-gon minimal surface patches. (C) An example of an 8-gon minimal surface patch in a unit cell of the face-centered cubic lattice. (D) An example of a 4-gon minimal surface patch in a unit cell of the octet-truss lattice.

Table 1
The designed dimensions of the unit cells in the six different groups. From top to bottom the non-auxetic structures without the surfaces (C), with the surfaces and slits (CS), and with the surfaces without the slits (CWS). Followed by the auxetic structures without the surfaces (A), with the surfaces and slits (AS), and with the surfaces without the slits (AWS).

Type	a [mm]	b [mm]	θ [°]	Relative Density
C	1.95	1.30	115	0.10
CS	1.95	1.30	115	0.12
CWS	1.95	1.30	115	0.13
A	1.95	1.30	65	0.20
AS	1.95	1.30	65	0.23
AWS	1.95	1.30	65	0.27

graphics software Blender (version 2.81, Blender Foundation, Amsterdam, The Netherlands). The permeability (*k*) is often considered a key parameter in bone tissue engineering, since it affects the nutrient and oxygen flow inside the scaffold and hence the *in vivo* bone formation. It best represents all other geometrical features (*e.g.*, pore shape, pore size and pore interconnectivity), and may be analytically calculated using the Kozeny equation [24]:

$$k = \frac{1}{C_k}\left(\frac{\phi^3}{S_s^2}\right)$$

This equation describes its relation with the volume fraction, or porosity (ϕ), and the specific surface area ($S_s = S/L^3$). The normalized effective permeability was found to be directly proportional to this geometrical relation, in which *L* describes the width of the box bounding the unit cell [12,24]. In the absence of the Kozeny constant, the calculated values give an impression of the relative differences in permeability between the designs.

After printing, the dimensions of the specimens were measured using a caliper, while a laboratory scale (Sartorius AG, Göttingen, Germany, 0.1 mg accuracy) was used to weigh the specimens. The dry weighing technique was then used to determine the as-manufactured relative density of the specimens, for which the weight of the specimens was divided by the weight of a solid Ti-6Al-4V object with similar dimensions and a density of 4.43 g/cm^3. The specimens were assessed on their quality using scanning electron microscopy (SEM) (JSM-IT100LA, JEOL, Tokyo, Japan). This was primarily done to gain a better perspective on the amount of surface area that was added to the lattices, as well as the quality and openness of the applied slits. The patches were visualized with a beam energy of 10–20 kV and a working distance of 14–30 mm.

2.4. Mechanical testing

2.4.1. Experimental testing

The *quasi-static* mechanical properties were obtained according to ISO 13314:2011 [25], once the data were corrected for machine compliance using the 'direct technique' [26]. The elastic modulus was then calculated in the linear region of the stress-strain curve between 30% and 70% of the first maximum compressive strength (FMCS). The latter corresponds to the first local maximum in the stress-strain curve. Finally, the compressive yield strength (σ_y) was measured at 0.2% compressive strain.

Full-field strain measurements were performed using the digital image correlation (DIC) technique, especially to gain insight in the Poisson's ratio of the different structures. To make sure the printed Ti-6Al-4V structures had a sufficiently high number of surface landmarks, a speckle pattern was added. The specimens were first spray-painted in black. The front surface was then stamped in white. Finally, a black random and *unique* speckle pattern was added with an airbrush.
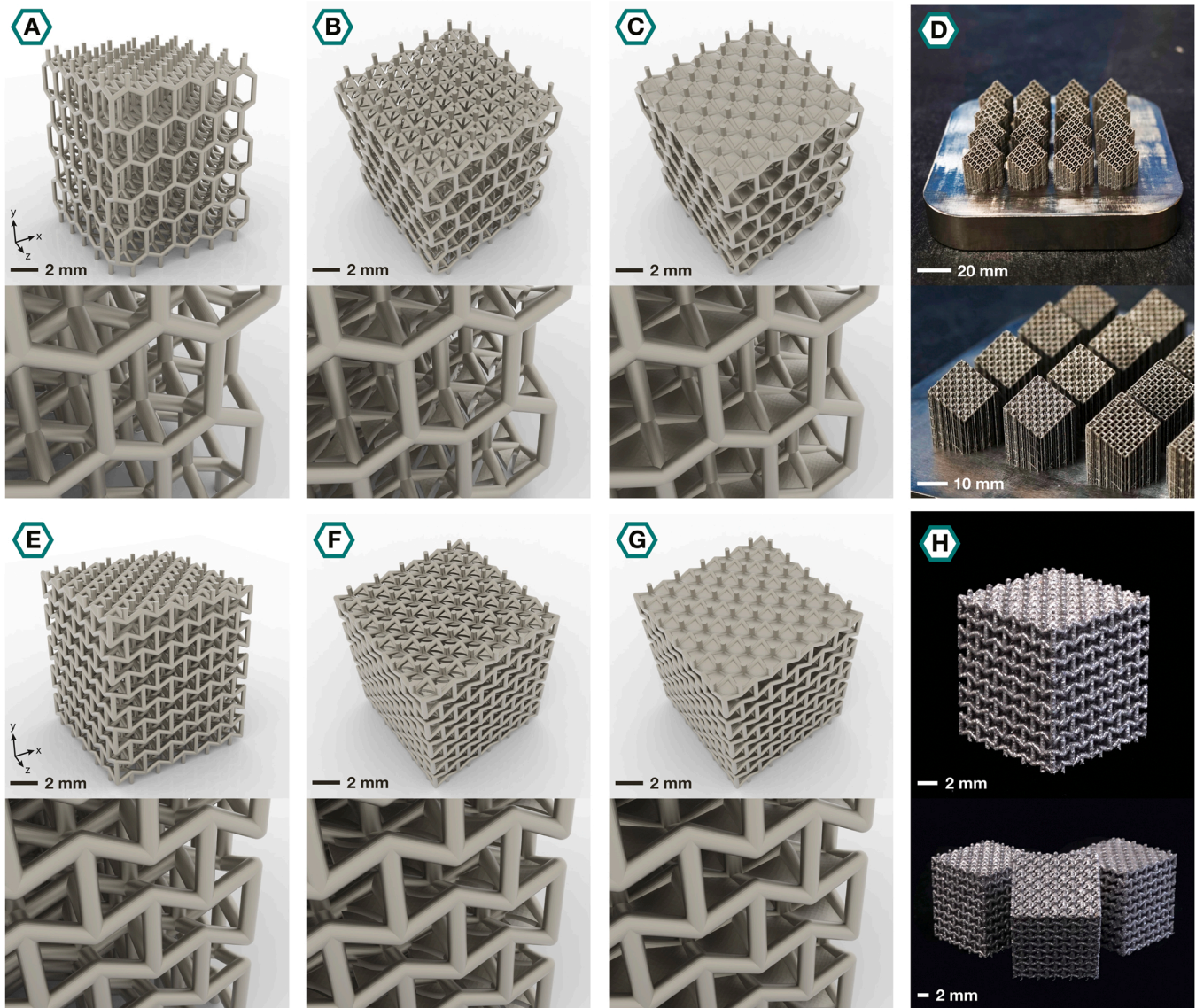
Fig. 2. A three-dimensional representation of the six meta-biomaterials studied here, presented through their computer-aided designs and as-manufactured parts. (A) C, (B) CWS, and (C) CS as well as their as-manufactured counterparts (D). (E) A, (F) AWS, (G) AS, and their as-manufactured counterparts (H).

Table 2
Additive manufacturing parameters for printing both auxetic and non-auxetic meta-biomaterials.

	Slice height [μm]	Exposure time [μs]	Point distance [μs]	Laser power [W]	Hatch strategy	Hatch distance [μm]
Contour	50	20	10	88	–	–
Hatch	50	5	10	88	90° alternating	150

The full experimental set-up was then calibrated using the VicSnap software (Correlated Solutions Inc., Irmo, USA). During the compression tests, two 4-Megapixel digital cameras (Limess, Krefeld, Germany) captured the front surface at a frequency of 1 Hz. The displacement and strain fields were calculated in the image analysis software Vic3D (Correlated Solutions Inc., Irmo, USA). The relative displacements of a group of unit cells in the middle of the structure were used to calculate the Poisson's ratio ($\nu_{yx} = -\varepsilon_{xx}/\varepsilon_{yy}$) in the linear region of the stress-strain curve [1,3,27]. The directional strain values (*i.e.*, ε_{xx} and ε_{yy}) were calculated using the coordinates of twelve vertices at different stages of deformation. Once a plateau was reached, the last ten values were used to calculate the average value of the Poisson's ratio.

The specimens were axially compressed using a mechanical testing machine (MTS, Eden-Prairie, USA). They were compressed for 5 mm with a displacement rate of 1 mm/min. The experiments were performed in two directions, standing upright and at a 90-degree angle (*i.e.*, tilted (T), used as a subscript to label the results). For both configurations, five specimens of each design were tested. In the tilted position the patches are oriented in the direction of the applied load, whereas they are perpendicular to the direction of loading in the upright position.

2.4.2. Computational modelling

To compute the effective elastic modulus and the elastic anisotropy of the different non-auxetic and auxetic designs, a linear elastic finite element-based computational homogenization code in Matlab was used [28]. First, the (non-cubic) unit cell designs were converted to a voxelized representation using the triSurf2Im code in the Gibbon toolbox, employing cubic voxels [23]. Next, the homogenized stiffness tensor C^* was computed by performing six independent linear-elastic finite element (FE) simulations using an isotropic linear elastic material model, periodic boundary conditions and eight-node hexahedral

elements. The six linear-elastic simulations were performed by applying macroscale unit strains to the unit cells in the six directions: three simulations in axial loading (x,y, and z), and three simulations in shear loading (xy, xz, yz). A mesh convergence study (on the basis of effective elastic modulus E_{11}^*) was performed, and a discretization of 120 voxels (20 μm in size) in the minimum dimension, with a proportional number of voxels in the maximum dimension, was found to be sufficient. The input material properties for the simulations were calculated in a compression test on ten solid cylinder specimens ($\varnothing = 10$ mm, height = 15 mm). The structures were printed in the same configuration as the auxetic and non-auxetic meta-biomaterials. The data were corrected for machine compliance [26], which resulted in an elastic modulus of 30.2 GPa and a Poisson's ratio of 0.3. Our primary simulation interest lies in studying the normalized effective stiffness (normalized with respect to the bulk material stiffness), which is irrespective of the choice of the elastic modulus. Using the preconditioned conjugate gradient solver in Matlab (tolerance = 10^{-8}), the FE equations were solved, and the effective stiffness tensor was obtained. The effective elastic modulus in various directions was then obtained from the effective compliance tensor S^* (the inverse of C^*) and a rotation matrix and was plotted as a 3D surface. Normalized effective stiffness values were calculated using the bulk material modulus (E_s).

2.4.3. Statistical Analysis

All statistical analyses were performed using GraphPad Prism 9 (GraphPad Software, CA, USA). Unless otherwise indicated, the statistical tests correspond to ordinary one-way ANOVA followed by the Tukey's multiple comparisons test. The differences were considered statistically significant for $p < 0.05$.

3. Results

3.1. Morphological characteristics

All six designs were successfully manufactured, and closely matched their designed dimensions (Fig. 2, Table 3). The relative density values were obtained using the dry-weighing technique and ranged between 0.16 and 0.30 (Table 3). In all cases, the relative density values were larger than their designed values. Most of the weight was added to the 'simple' lattice structures, while differences between the designs were small.

The 'slits' that were applied to the patches of designs CS and AS were clearly visible throughout the specimens (Figs. 3A and 3C). The images do suggest that some ends of the patches may be connected to the surrounding struts through adherent powder particles. The designs CWS and AWS were designed 'without slits', which was also successfully translated to the as-manufactured specimens (Figs. 3B and D). With the addition of these patches, the surface area of the lattices was increased by 20–25% (Table 3). The largest surface area was found for the designs with 'slits' (CS and AS), while the smallest surface area was measured in the simple lattices (C and A) (Fig. 3). The simple lattices exhibited a higher permeability than their counterparts with surface patches (Table 3). A slight increase in permeability was observed in CWS, with respect to CS.

3.2. Mechanical properties

For each of the designs the mean stress-strain curve has been presented in Fig. 4. Typically, the stress-strain curve of porous biomaterials exhibits a linear region followed by a plateau region with fluctuations. The fluctuations generally match the subsequent collapse of individual layers inside the structure. These collapses were clearly visible in the designs with surface patches, but without the slits (i.e., CWS$_{(T)}$ and AWS$_{(T)}$, with (T) used to refer to both testing configurations) (Fig. 4). CWS$_{(T)}$ exhibited drop-to-zero stress evolution patterns, which happen in between the collapse of layers and subsequent take-up of the load by another layer, allowing the stress to increase again. In the upright position, this also holds true for the other two non-auxetic designs (i.e., C and CS). In the titled configuration, C$_T$ and CS$_T$ failed along a diagonal shear line, while CWS$_T$ first exhibited buckling before the first layer collapsed. The fluctuations were less extreme in the auxetic designs (i.e., A and AS) with smaller drops in the stress. This was especially the case for the specimens tested in the tilted position (i.e., A$_T$ and AS$_T$), in which the stress gradually decreased with strain, exhibiting a diagonal shear line (Fig. 5B). The stress only started to recover towards the end of the test, but no other maxima were reached.

The mechanical properties were found to increase with the relative density (the addition of surfaces). However, these differences were mostly non-significant in the upright configuration (Table 4, Fig. 5). The only significant difference in the stiffness was found between C and CWS, with CWS exhibiting a 13% higher elastic modulus. In the tilted position, the designs with surfaces and without the slits (CWS$_T$ and AWS$_T$) exhibited a significant increase in both stiffness and strength. The CWS$_T$ design exhibited an elastic modulus of 3088.16 ± 98 MPa, which is almost twice as high as the stiffness measured for the other two non-auxetic meta-biomaterials ($p < 0.0001$ for CWS$_T$ vs. C$_T$ and for CWS$_T$ vs. CS$_T$) (Fig. 5C). A similar increase can be observed for its strength (Table 4). The AWS$_T$ design showed a similar increase in stiffness, with an elastic modulus of $11,192.42 \pm 901$ MPa, as compared to 4892.60 ± 257 MPa ($p < 0.0001$) and 5347.60 ± 159 MPa ($p < 0.0001$) for A$_T$ and AS$_T$, respectively (Fig. 5D). The non-auxetic designs showed a decrease in their stiffness and strength when tilted by a 90° angle, except for CWS$_T$. The auxetic meta-biomaterials exhibited an increase in stiffness and strength, once tilted.

The average values of the Poisson's ratio show that the structures made using the hexagonal honeycomb unit cell (i.e., non-auxetic) expand under compression, thus having a positive Poisson's ratio (Table 4, Fig. 5A and E). No significant differences were found between the simple lattices (C$_{(T)}$) and the lattices with surfaces and slits (CS$_{(T)}$) in terms of their Poisson's ratio. As compared to the design without surfaces, the design with surfaces and without the slits had a significantly lower Poisson's ratio in the upright position ($p < 0.0001$ for CWS vs. C), and a significantly higher value in the tilted configuration ($p < 0.01$ for CWS$_T$ vs. C$_T$). C$_T$ and CS$_T$ both exhibited a smaller value of the Poisson's ratio as compared to their counterparts in the upright configuration. CWS$_T$, on the other hand, showed an increase in its Poisson's ratio as compared to CWS (Fig. 5E). The structures based on the re-entrant hexagonal honeycomb, which were designed to have a negative Poisson's ratio (i.e., auxetic), indeed exhibited a lateral contraction in

Table 3

The as-manufactured dimensions, relative density values, surface area and permeability predictions of the six different groups.

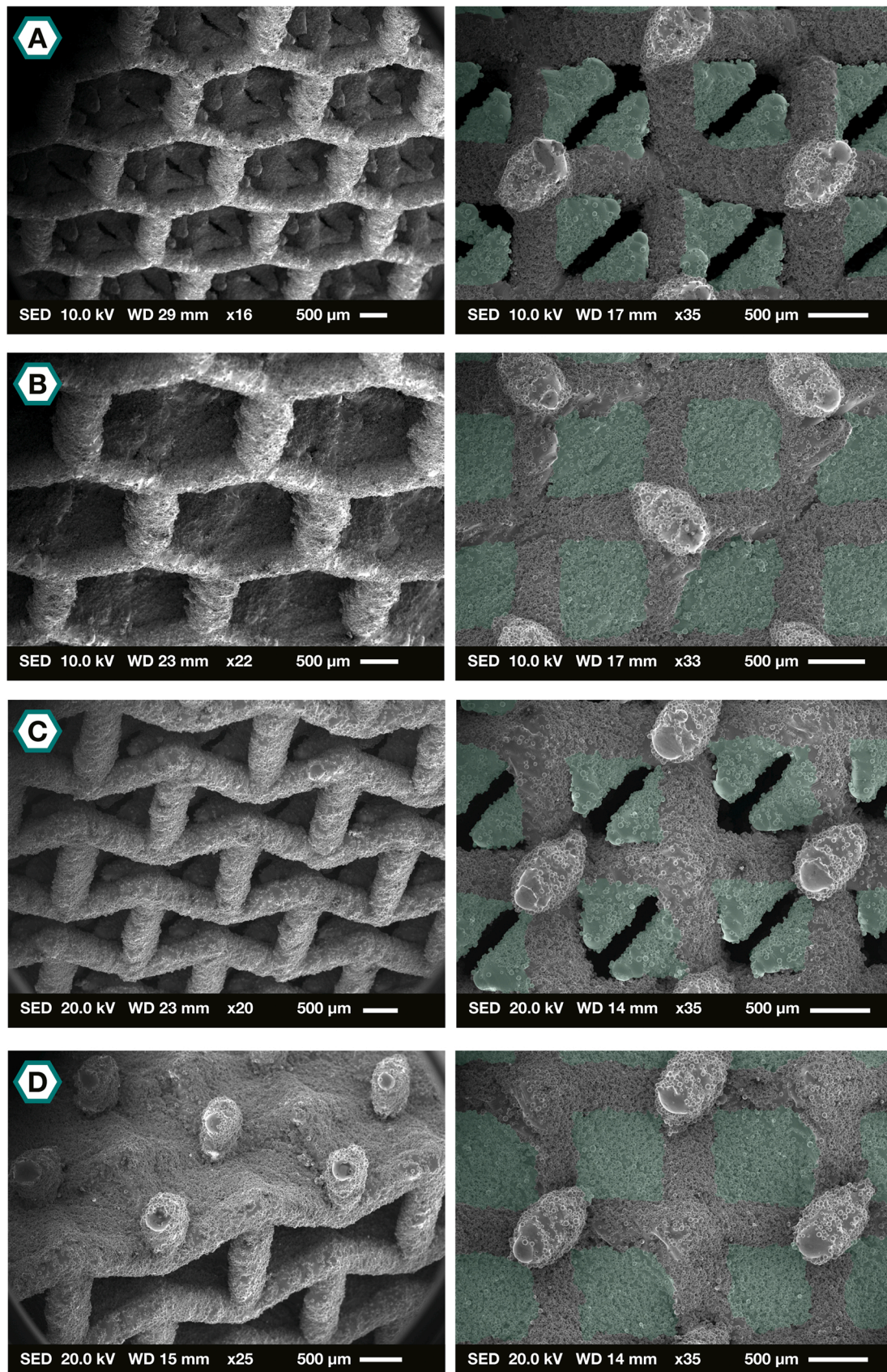| Type	Length [mm]	Width [mm]	Height [mm]	Relative Density	Surface Area [mm²]	$\dfrac{\phi^3}{(S/L^3)^2}$
C	12.49 ± 0.03	12.52 ± 0.04	15.26 ± 0.08	0.16 ± 0.001	2432.61	0.33
CS	12.50 ± 0.03	12.52 ± 0.07	15.29 ± 0.05	0.17 ± 0.001	2999.36	0.20
CWS	12.53 ± 0.10	12.51 ± 0.08	15.32 ± 0.10	0.18 ± 0.003	2872.44	0.22
A	12.61 ± 0.10	12.62 ± 0.05	14.28 ± 0.06	0.26 ± 0.004	3800.87	0.10
AS	12.54 ± 0.07	12.64 ± 0.07	14.22 ± 0.04	0.29 ± 0.003	4737.38	0.06
AWS	12.56 ± 0.06	12.62 ± 0.06	14.26 ± 0.07	0.30 ± 0.004	4531.23	0.05

Fig. 3. The structure and surface quality of the different designs observed using SEM. (A) CS × 16 and × 35. (B) CWS × 22 and × 33. (C) AS × 20 and × 35. (D) AWS × 25 and × 35. The colored areas highlight the additional surface area in each of the designs.
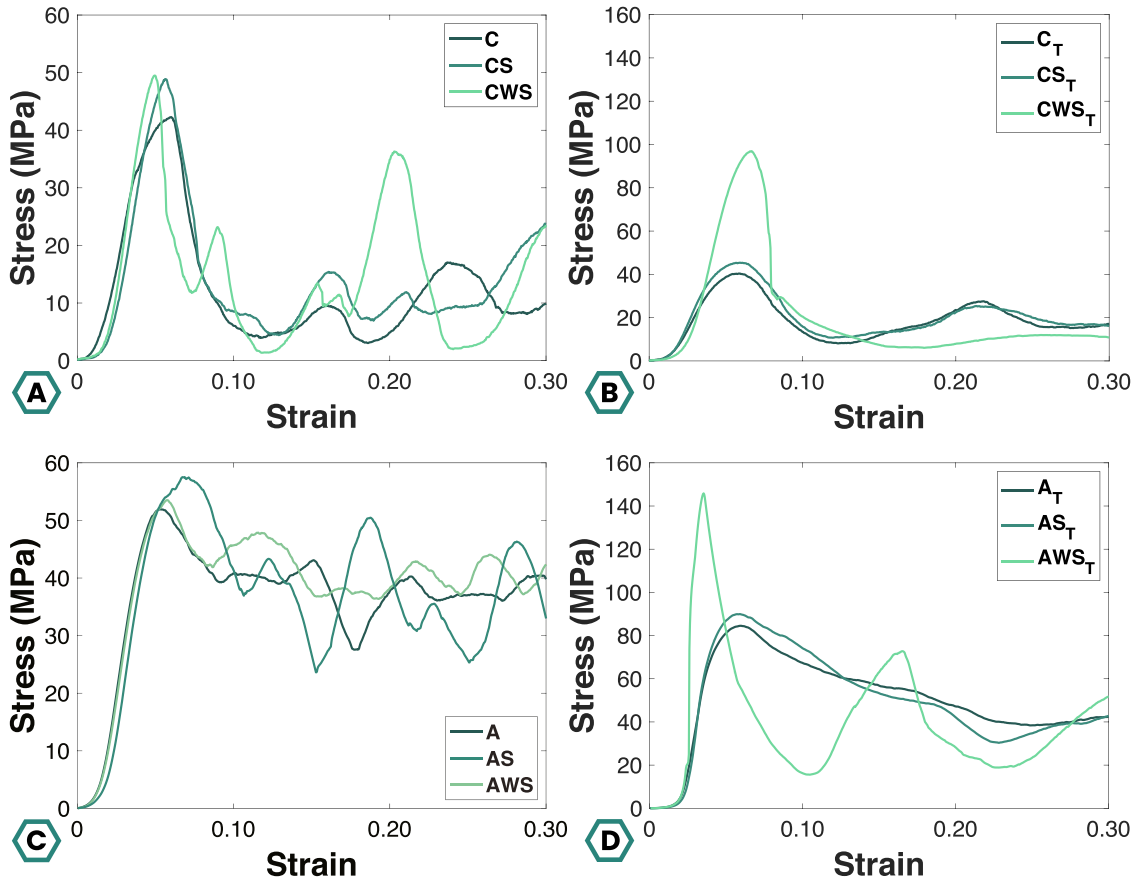
Fig. 4. The average stress-strain curves of (A) the non-auxetic designs in the upright position, (B) the non-auxetic designs in the tilted position, (C) the auxetic designs in the upright position, and (D) the auxetic designs in the tilted position.

response to the axial compression (Figs. 5B and 5 F). In both configurations, A and AS exhibited similar values of the Poisson's ratio. The differences with AWS were significant in the upright configuration ($p < 0.0001$), showing a notably smaller lateral contraction. Once tilted, the NPR of A_T and AS_T decreased, whereas the value of AWS_T increased (Fig. 5F).

The computational homogenization analyses of the effective elastic modulus revealed that the standard non-auxetic and auxetic unit cells are elastically anisotropic, which is typically found in many strut-based lattices (Fig. 6A and C). For example, the hexagonal honeycomb unit cell shows a relatively high effective stiffness in the three main orthogonal directions with the highest stiffness obtained in the primary loading direction ($E_x^* > E_y^* = E_z^*$). The effective stiffness rapidly decreases for off-axis loading, resulting in the stellated shape of the elastic modulus surface (Fig. 6A). The standard auxetic design exhibited a similar behavior, albeit with a higher stiffness in the other directions (Fig. 6C, $E_y^* = E_z^* > E_x^*$). As expected, and as confirmed by the experimental test results, the effective stiffness and degree of elastic anisotropy remains virtually constant when surfaces with slits are added to the designs. However, the addition of surfaces without slits substantially altered the anisotropic elastic behavior (right panels in Fig. 6A and C). Specifically, the anisotropy in the *yz*-plane was reduced, and a disk-like shape appeared in the surface representing the elastic modulus. Additionally, the presence of surfaces without slits caused an increase in the predicted effective stiffness in the primary loading direction, E_x^*, confirming the experimental observations (Figs. 6B and 6D). The normalized effective stiffness values were higher for the non-auxetic designs as compared to the auxetic designs in the upright position. Once tilted, the auxetic designs outperform the non-auxetic designs in terms of stiffness (Table 5). The primary purpose of our computational analyses was to study the

elastic anisotropy and to confirm the experimentally observed effects of adding surfaces with or without slits to the strut-based designs, which is why we were mainly interested in the normalized effective stiffness (E^*/E_s). As described before, our simulations were of the linear elastic type, meaning that the choice of E_s is immaterial to the obtained values of the normalized effective stiffness values. A prediction of the dimensional effective stiffness values (*i.e.*, the non-normalized E^* values) were computed using the material properties of solid Ti-6Al-4V cylinders (Table 5). In general, these predictions capture similar trends as the experimentally observed values. However, the predicted values for E^* are consistently smaller than their experimental counterparts. This could indicate that the bulk material stiffness (E_s) was different for non-auxetic designs as opposed to the auxetic designs, which could be a result of the different design and design-dependent manufacturing defects [29–31].

4. Discussion

We proposed a new strategy to decouple the mechanical properties and available surface area in metallic meta-biomaterials. Both auxetic and non-auxetic meta-biomaterials were designed and additively manufactured, either with or without the addition of surfaces. The results of both the computational models and the experimental tests show that the addition of rationally designed surfaces can increase the surface area independent of the mechanical properties.

4.1. Morphological characteristics

Recent advances in additive manufacturing have enabled the fabrication of complex three-dimensional shapes, prompting the
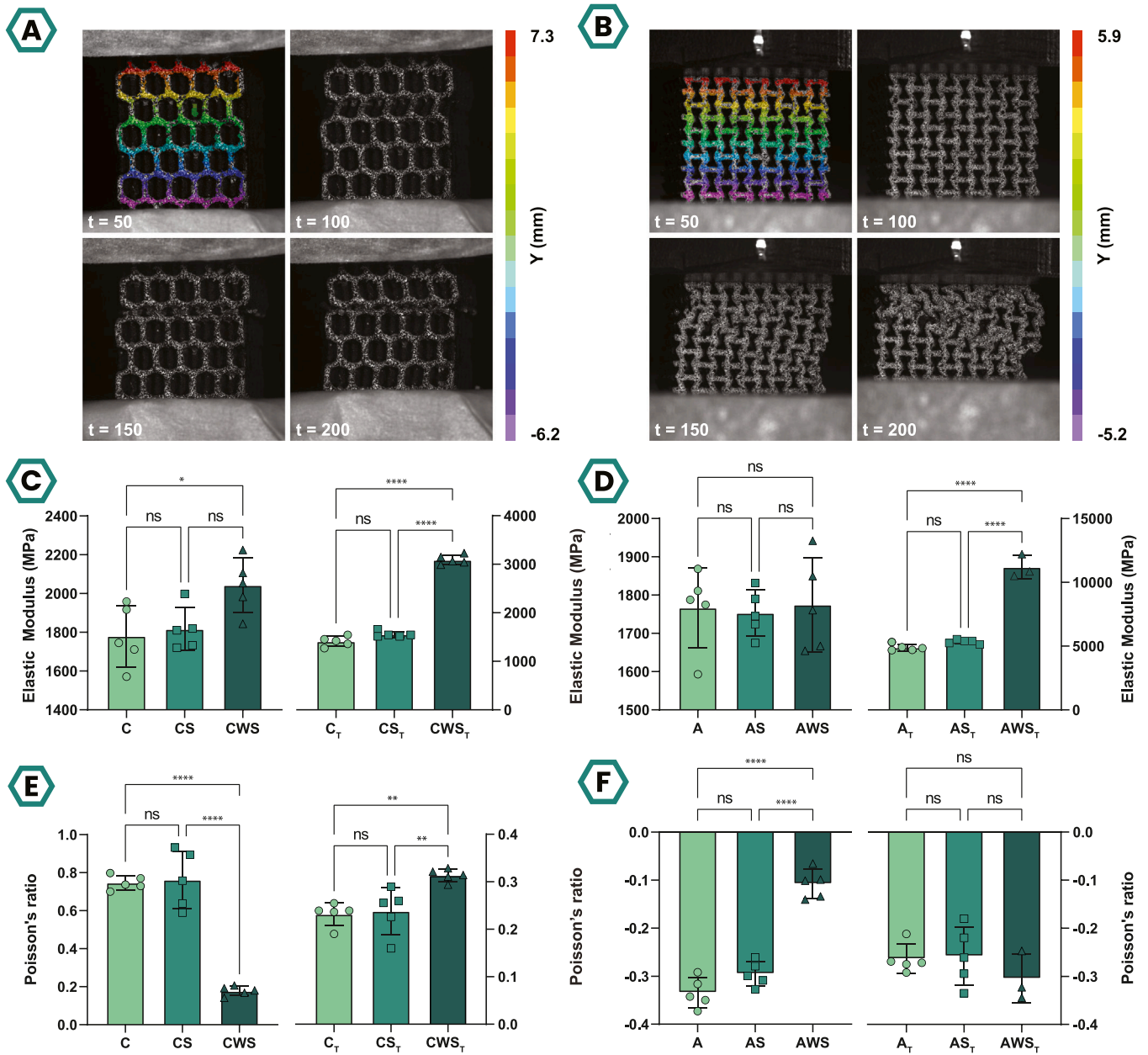
Fig. 5. Experimental results of the *quasi-static* compression tests in both configurations. (A) Deformation of CWS over time with an example of a DIC read-out. (B) Deformation of AS_T over time with an example of a DIC read-out. (C) Elastic modulus of the non-auxetic meta-biomaterials. (D) Elastic modulus of the auxetic meta-biomaterials. (E) Poisson's ratio of the non-auxetic meta-biomaterials. (F) Poisson's ratio of the auxetic meta-biomaterials. $* : p \leq 0.05$, $**: p \leq 0.01$, $*** : p \leq 0.001$, $****: p \leq 0.0001$, ns: not significant.

development of many complex 'designer materials' [1–3,12] of which the meta-biomaterials in this study are the newest examples. These biomaterials can simultaneously satisfy multiple design requirements, including a high volume of pore spaces, vast surface areas, tailored anisotropic elasticity tensors, bone-mimicking elastic moduli, and negative values of the Poisson's ratio. Nevertheless, it remains a challenge to successfully print a geometry with so many overhanging structures. The geometries were, therefore, built at an angle with respect to the build plate. The as-manufactured relative density values were higher than the designed values. This is likely due to the imperfections (*e.g.*, powder adhesion, over-melting, strut thickness heterogeneity) that are inherent to metal printing processes [32–34]. The adhering powder particles may limit the displacement of the surfaces relative to the struts. In some cases, the surfaces may even be fused with the surrounding struts, although we did not detect any such merger in our SEM images.

Even if present, these connections are expected to be relatively weak and therefore easy to detach upon loading.

As intended, the surface area of the structures was substantially increased through the addition of rationally designed surface patches. Surprisingly, the largest surface area was reported for the designs with surfaces and with slits (*i.e.*, CS and AS). The width of the slits was smaller (175 μm) than the thickness of the surfaces (200 μm), meaning that their inclusion has increased the surface area instead of decreasing it. These designs, therefore, feature a slightly larger surface area than the designs with surfaces and without the slits (*i.e.*, CWS and AWS) (Table 3). This slight advantage in terms of additional surface area ($\approx$ 200 mm^2) is, however, only present in the designs where the slit width is smaller than the surface thickness.

Table 4
The *quasi-static* mechanical properties of the six different designs in the upright and tilted (T) configurations.

Type	Elastic modulus (MPa)	FMCS (MPa)	Yield strength (MPa)	Poisson's ratio
C	1780.55 ± 158	49.39 ± 2	42.52 ± 1	0.747 ± 0.04
C_T	1412.10 ± 103	41.42 ± 2	34.32 ± 1	0.232 ± 0.02
CS	1816.07 ± 111	51.62 ± 1	44.43 ± 2	0.762 ± 0.15
CS_T	1556.06 ± 60	45.70 ± 2	38.05 ± 2	0.238 ± 0.05
CWS	2042.50 ± 142	52.08 ± 2	46.67 ± 3	0.178 ± 0.02
CWS_T	3088.16 ± 98	97.86 ± 4	85.39 ± 3	0.313 ± 0.01
A	1766.92 ± 104	52.88 ± 3	46.02 ± 2	-0.335 ± 0.03
A_T	4892.60 ± 257	84.83 ± 3	68.19 ± 2	-0.264 ± 0.03
AS	1753.04 ± 60	53.73 ± 1	45.95 ± 1	-0.295 ± 0.03
AS_T	5347.60 ± 159	90.49 ± 2	73.36 ± 1	-0.258 ± 0.06
AWS	1774.64 ± 122	57.97 ± 2	48.87 ± 3	-0.108 ± 0.03
AWS_T	11,192.42 ± 901	147.09 ± 2	105.65 ± 1	-0.305 ± 0.05

4.2. Geometry-property relationships

The fluctuations that were observed in the stress-strain curves of both the auxetic and non-auxetic meta-biomaterials correspond to the successive failure of individual layers. The layer containing the weakest link collapses first, after which the stress will increase until another link fails, and so on. In the tilted configuration, the number and intensity of these fluctuations decreased. In this configuration, there are no struts oriented in the loading direction, which means the deformation is guided by the bending of the diagonal struts. As a result, a diagonal shear profile could be observed. In the designs with surfaces and without the slits (*i.e.*, CWS_T and AWS_T) the surfaces are oriented in the loading direction, thus contributing to the mechanical properties of the material. The buckling mechanism that was observed in CWS_T right before failure, is a direct result of the surface patches being axially compressed.

The mechanical properties of the auxetic and non-auxetic meta-biomaterials significantly increased once fully closed surface patches were added in the loading direction. The addition of these solid "walls" enhances the load-carrying capacity of the structures. With the slits in place, the surfaces are no longer connected to all four surrounding struts. Instead, they were connected to only one strut, meaning they could move around. Under such circumstances, the load is carried by the lattice alone. Due to powder adhesion, some of the slits may have been partially or fully fused with the surrounding struts. This could explain the relatively high standard deviations found for some of the meta-biomaterial properties, which may also be caused by the two opposing surfaces touching each other upon deformation.

In the absence of the surface patches, the mechanical performance of the non-auxetic meta-biomaterials is comparable for both configurations, with a small drop in the compressive stiffness (−21%) and strength (−19%), once tilted. This can be explained by the absence of vertically oriented struts in C_T. Similar results have been reported in the literature and were also confirmed by our simulations (Table 5) [35]. According to both the experimental and computational results, the auxetic meta-biomaterials have a significantly higher load-bearing capacity in the tilted configuration (+277% and +148%, respectively). In A, the applied load is directly responsible for the collapse of the re-entrant hexagonal honeycomb, whereas it acts on the horizontal struts in A_T. Similar observations are reported in the literature [35,36]. In their presented form, the auxetic meta-biomaterials outperform the non-auxetic meta-biomaterials in the tilted configuration. In general, the auxetic meta-biomaterials are more compliant in the presented loading direction as compared to their non-auxetic counterparts (assuming a similar relative density) [1,37]. The observed difference is, therefore, a direct result of the higher relative density of the auxetic designs (Table 3). Once normalized by their volume, the non-auxetic meta-biomaterials do exhibit a higher stiffness (Table 5).

The presence or absence of the slits clearly affects the computationally predicted surfaces of the elastic modulus. With the slits present, the structure effectively exhibits the same behavior as the designs without surfaces, resulting in a nearly identical elastic modulus surface and predicted effective stiffness. When no slits are present, however, the stiffness in all directions within the *yz*-plane drastically increases, and the elastic modulus surface is altered substantially. Indeed, the presence of surfaces without slits essentially adds plate-like elements to the unit cell that cause the unit cell to exhibit near isotropy when loaded along in-plane directions. These insights confirm that the slits are not only necessary to maintain the overall effective stiffness of the strut-based lattices in the main loading directions, but also to preserve their anisotropic response.

The computationally predicted values of the effective stiffness are substantially lower than their experimental counterparts. The input material properties were determined in the main printing direction, but once a part is printed at an angle with respect to the build plate, the mechanical properties generally decrease [29,38]. The struts in our designs are oriented in multiple directions, which means the overall print quality could also be higher. Fitting the predicted effective stiffness of the standard auxetic design to the corresponding average experimental value, resulted in $E_s = 81.48$ *GPa*. This suggests that the quality of the solid cylinders is about a factor 2–3 lower than the overall quality of the auxetic and non-auxetic meta-biomaterials. Overhanging structures, or those printed diagonally, push the boundaries of the SLM process and may consequently be of inferior quality [29,32–34,38,39]. Fortunately, various efforts are made to effectively predict the impact of printing imperfections on the mechanical performance of additively manufactured lattice structures [40–42].

The Poisson's ratio of the non-auxetic meta-biomaterials is generally higher in the upright configuration, showing a bigger lateral expansion in response to axial compression [35]. The absolute values of the Poisson's ratio follow a similar trend as the one we found in an earlier study on hexagonal honeycomb lattices [1]. These absolute values drastically decrease once fully closed surface patches are present. The results suggest that these surface patches hinder the bending-dominated deformation mechanism that relies on the hinging of cell ribs. In the tilted configuration, the Poisson's ratio of CWS_T is again significantly different from the other two designs. In this configuration, the surface patches seem to enhance the lateral deformation. This can be explained by their stiffer response, which forces the lateral nodes to move outwards upon axial compression. The auxetic meta-biomaterials exhibited NPR values in both configurations. In general, a slightly larger lateral contraction was observed when they were tested in the upright position. Similar observations are reported in the literature, although differences decrease when θ increases [35,36,43]. Absolute values were found to overlap the computationally derived values published in an earlier study [44]. The differences between the designs were generally non-significant, except for the Poisson's ratios in the upright configuration. A significant decrease in the NPR was observed once the surface without the slits were added. This may again be explained through the deformation mechanism of the re-entrant hexagonal honeycomb, which is more restricted once struts are connected through a rigid surface. In the tilted configuration, the surfaces work with the deformation mechanism, instead of against it. The Poisson's ratio was, therefore, not affected by the addition of the rationally designed minimal surface patches, whereas the surfaces without slits did significantly alter the deformation pattern of the structures in at least one direction.

4.3. Biological performance

The term osseointegration is used to describe the integration of the implant in its surrounding bony environment and was first introduced by Brånemark and co-workers in 1976 [45]. After years of research, we now know that the osseointegration process can be influenced by a variety of factors, involving both the environment and the design of the implant itself [46]. The latter has been the main focus of this research and can be broken down into multiple aspects including the
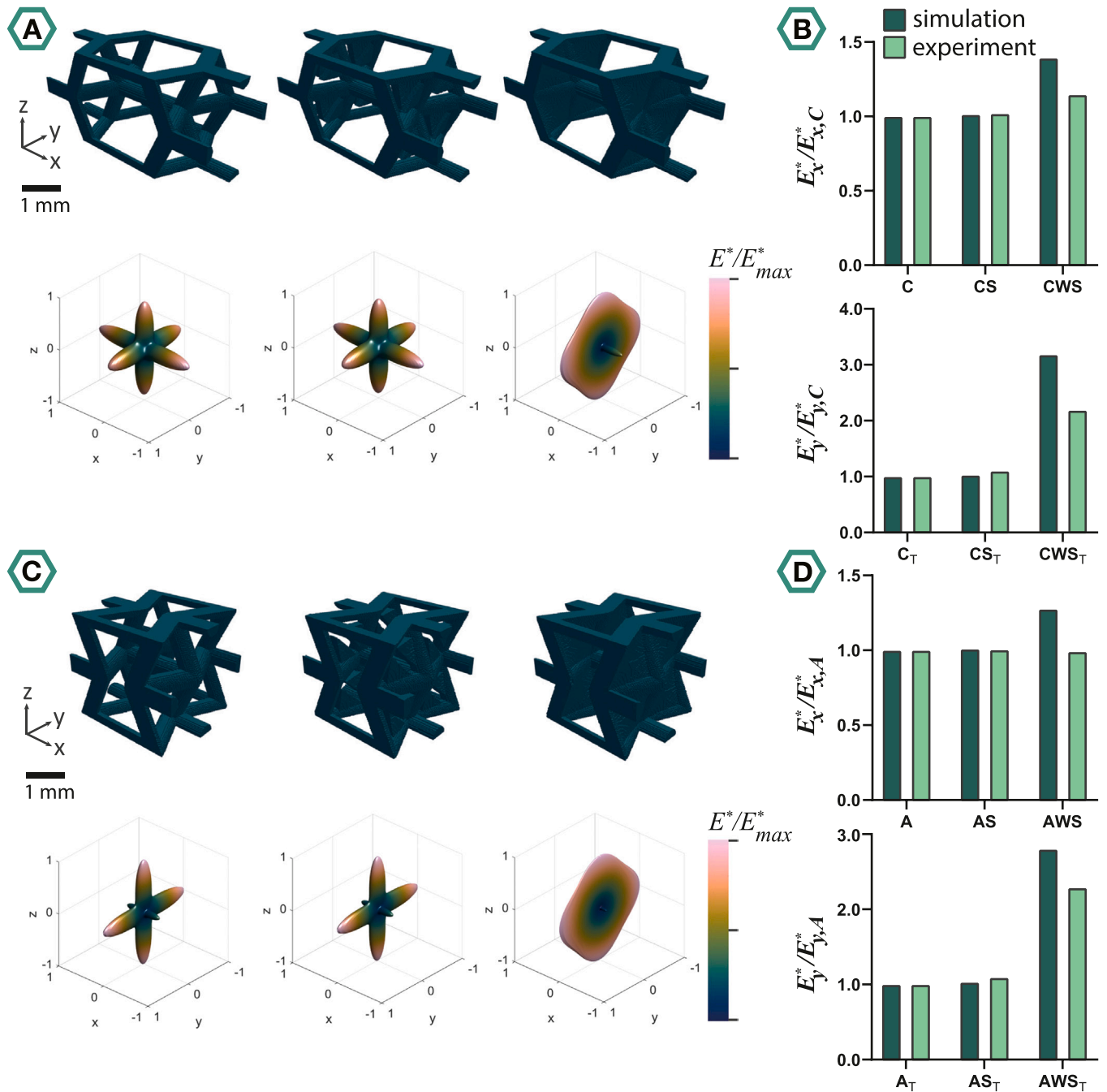
Fig. 6. Effective stiffness obtained through computational homogenization. (A) Voxelized representations (top row) and corresponding effective elastic modulus surfaces (bottom row), for the C (left), CS (middle), and CWS (right) designs. Every elastic modulus surface is colored according to the magnitude of the effective stiffness in any particular direction, normalized with respect to the maximum effective stiffness of that design (E^*/E^*_{max}). (B) Comparison of the experimental and computational effective stiffness, normalized with respect to the stiffness of the design without surfaces. (C)-(D) Similar to (A)-(B) but for the auxetic designs.

biocompatibility, topology, macro-/micro-architecture, and mechanical properties [46–48]. Porous bone scaffolds are shown to be very effective in the treatment of critically sized bone defects, as their mechanical properties match those of the surrounding bony tissue. Furthermore, the interconnected network of pores allows for deep tissue integration. This can not only solve the longstanding problem of stress shielding, but also enhance osseointegration and therefore improve the long-term fixation of the implants [49]. The bone-implant interface in porous scaffolds has been, indeed, found to be much stronger than the one created in solid bone implants [47]. The porous meta-biomaterials that were proposed in this study serve the same purpose, providing a rich network of pore spaces to improve the mechanical interlocking of the implant with the surrounding bone. Through the rational design of the surface patches, the surface available for cell adherence was increased without substantially changing the mechanical properties of the developed meta-biomaterials. The imperfections cause by the additive manufacturing process, such as the surface roughness, may further improve the mechanical interlocking by increasing the number of cell/protein adhesion sites [50].

The macro- and micro-architecture of the scaffold go hand in hand with the permeability, which is of great importance for cell infiltration and sustenance [51]. Bigger pores are often preferred during progressive growth, since they will provide enough space for nutrients and oxygen to pass through. Smaller pores, on the other hand, will easily get occluded,

Table 5

The simulated effective stiffness values (E*) for all six designs in the normal (*x*) and tilted (*y*) configurations. Both the normalized (E*$_x$ / E$_s$) and dimensional (E*$_x$) values are provided. The latter were obtained by multiplying the normalized values with the estimated bulk material elastic modulus E$_s$ = 30.2 GPa, which was obtained from the compression tests on solid Ti-6Al-4V cylinders.

Type	E*$_x$ / E$_s$	E*$_x$(MPa)	E*$_y$/ E$_s$	E*$_y$(MPa)
C	0.0318	960.36	0.0282	851.64
CS	0.0322	972.44	0.0290	875.80
CWS	0.0443	1337.86	0.0898	2711.96
A	0.0217	655.34	0.0607	1833.14
AS	0.0219	661.38	0.0626	1890.52
AWS	0.0277	836.54	0.1702	5140.04

but may also prevent or slow the continuous flow of fluid, thereby improving cell adhesion [51]. With the rationally designed minimal surface patches in place, the permeability is somewhat decreased, but the slits will still allow the passage of nutrients and oxygen throughout the scaffold. Furthermore, the rational introduction of the patches increase the tortuosity, which will improve the delivery of oxygen and nutrients to every location in the structure [52]. This is not the case in the designs with the fully closed surface patches, where the pore inter-connectivity is significantly affected by the presence of these solid walls. Moreover, our design approach generally offers several patch configurations for a single strut-based lattice (Fig. 1), implying that the permeability could be tuned independently from the mechanical properties by selecting the desired patch configuration (with slits) for a given strut-based lattice.

The auxetic and non-auxetic meta-biomaterials that were introduced here belong to the category of permanent implants. Ti-6Al-4V is a bio-inert metal with great corrosion resistance and adequate mechanical characteristics, but complete restoration of the tissue will never be achieved [13,14]. Researchers have, therefore, begun to investigate biodegradable materials, including metals. In biodegradable metals, the implant will provides sufficient mechanical support upon implantation, after which it will slowly degrade allowing the new healthy tissue to take over [53]. Given its favorable biocompatibility and suitable mechanical properties, magnesium has long been the focus of research in the development of biodegradable orthopedic metals [53]. Unfortunately, magnesium and its alloys also tend to degrade too fast in physiological environments. The corrosion properties of biodegradable metals have, therefore, been widely studied, to obtain the optimal degradation rate for full bone regeneration [54–56]. One could adjust the architecture of the scaffolds to alter their permeability and fluid flow and, hence, their biodegradation rate. A functionally graded density has, for instance, been found to affect the biodegradation behavior of AM iron scaffolds [57]. A similar effect could be achieved using the rationally designed minimal surface patches in this study. Their addition could be used to not only alter the exposed surface area, but also to tune the permeability of the scaffolds independent of their mechanical properties.

4.4. Future research

The specimens in this study were made from Ti-6Al-4V, which is biocompatible but still contains several hazardous alloying elements. The specimens were successfully manufactured with SLM, which could also process other types of metallic powders. The above-mentioned biodegradable metals, such as magnesium, iron, and zinc, could therefore easily be applied using the same strategy.

The permeability of the scaffolds has not been studied here but is highly relevant for the biological performance of both auxetic and non-auxetic meta-biomaterials. Future research should, therefore, focus on the influence of the applied surface patches on the fluid flow inside the scaffolds. One could then adjust the geometry of the unit cells or use the

surface patches that are presented in Fig. 1A-B, to obtain the most optimal circumstances for bone tissue regeneration.

5. Conclusions

A new design approach, in which minimal surface patches were added to both auxetic and non-auxetic lattices (which is generalizable to virtually any type of strut-based lattice), was presented to decouple the mechanical properties and available surface area of metallic meta-biomaterials. Slits were added to minimal surface patches to limit their contribution to the mechanical properties. Control groups were designed either without the surface patches or without the rationally applied slits. All designs were additively manufactured and mechanically characterized in the upright and 90° tilted configurations. Linear-elastic FE simulations were performed to predict the effective elastic moduli and anisotropic behavior of the different groups of meta-biomaterials. The results show that the rationally designed minimal surface patches substantially increase the available surface area without significantly affecting the mechanical properties in either direction. Without the slits, the addition of the minimal surface patches significantly increased the elastic modulus in the tilted configuration. The fully closed surfaces were also found to restrict the deformation behavior in the upright configuration, while increasing the absolute value of the Poisson's ratio once tilted. A similar behavior was observed in the computationally predicted stiffness values with degrees of increases that consistently exceeded those determined experimentally. This may be explained by the relatively high complexity of the designs that pushed the limits of the layer-based printing technique and may have resulted in inferior print quality and geometrical imperfections. Similar design strategies may be used to tune the rate of biodegradation in biodegradable metals or the permeability of meta-biomaterials in general.

CRediT authorship contribution statement

H.M.A. Kolken: Conceptualization, Methodology, Validation, Formal analysis, Investigation, Writing – original draft, Writing – review & editing, Visualization, Project administration, **S.J.P. Callens:** Conceptualization, Methodology, Software, Formal analysis, Writing – review & editing, Visualization, **M.A. Leeflang:** Methodology, Resources, Writing – review & editing, **M.J. Mirzaali:** Writing – review & editing, Supervision, **A.A. Zadpoor:** Resources, Writing – review & editing, Supervision.

Declaration of Competing Interest

The authors declare that they have no known competing financial interests or personal relationships that could have appeared to influence the work reported in this paper.

Acknowledgements

References

[1] H.M. Kolken, S. Janbaz, S.M. Leeflang, K. Lietaert, H.H. Weinans, A.A. Zadpoor, Rationally designed meta-implants: a combination of auxetic and conventional meta-biomaterials, Mater. Horiz. 5 (1) (2018) 28–35.

[2] F. Bobbert, K. Lietaert, A.A. Eftekhari, B. Pouran, S. Ahmadi, H. Weinans, A. Zadpoor, Additively manufactured metallic porous biomaterials based on minimal surfaces: a unique combination of topological, mechanical, and mass transport properties, Acta Biomater. 53 (2017) 572–584.

[3] H. Kolken, C. de Jonge, T. van der Sloten, A.F. Garcia, B. Pouran, K. Willemsen, H. Weinans, A. Zadpoor, Additively manufactured space-filling meta-implants, Acta Biomater. 125 (2021) 345–357.

[4] S.M. Kurtz, E. Lau, K. Ong, K. Zhao, M. Kelly, K.J. Bozic, Future young patient demand for primary and revision joint replacement: national projections from 2010 to 2030, Clin. Orthop. Relat. Res. 467 (10) (2009) 2606–2612.

[5] S. Kurtz, K. Ong, E. Lau, F. Mowat, M. Halpern, Projections of primary and revision hip and knee arthroplasty in the United States from 2005 to 2030, Jbjs 89, 4, 2007 780–785.

[6] I.J. Wallace, S. Worthington, D.T. Felson, R.D. Jurmain, K.T. Wren, H. Maijanen, R. J. Woods, D.E. Lieberman, Knee osteoarthritis has doubled in prevalence since the mid-20th century, Proceedings of the National Academy of Sciences 114(35) (2017) 9332–9336.

[7] Ž. Perić Kačarević, P. Rider, S. Alkildani, S. Retnasingh, M. Pejakić, R. Schnettler, M. Gosau, R. Smeets, O. Jung, M. Barbeck, An introduction to bone tissue engineering, Int. J. Artif. Organs 43 (2) (2020) 69–86.

[8] A.A. Zadpoor, Bone tissue regeneration: the role of scaffold geometry, Biomater. Sci. 3 (2) (2015) 231–245.

[9] M. Mirzaali, A. Caracciolo, H. Pahlavani, S. Janbaz, L. Vergani, A. Zadpoor, Multi-material 3D printed mechanical metamaterials: rational design of elastic properties through spatial distribution of hard and soft phases, Appl. Phys. Lett. 113 (24) (2018), 241903.

[10] S. Janbaz, M. McGuinness, A.A. Zadpoor, Multimaterial control of instability in soft mechanical metamaterials, Phys. Rev. Appl. 9 (6) (2018), 064013.

[11] D. Chen, X. Zheng, Multi-material additive manufacturing of metamaterials with giant, tailorable negative Poisson's ratios, Sci. Rep. 8 (1) (2018) 1–8.

[12] S.J.P. Callens, C.H. Arns, A. Kuliesh, A.A. Zadpoor, Decoupling Minimal Surface Metamaterial Properties Through Multi-Material Hyperbolic Tilings, Adv. Funct. Mater. 31 (30) (2021), 2101373.

[13] M. Niinomi, Recent metallic materials for biomedical applications, Metall. Mater. Trans. A 33 (3) (2002) 477–486.

[14] M. Niinomi, Mechanical biocompatibilities of titanium alloys for biomedical applications, J. Mech. Behav. Biomed. Mater. 1 (1) (2008) 30–42.

[15] R. Huiskes, R. Ruimerman, G.H. Van Lenthe, J.D. Janssen, Effects of mechanical forces on maintenance and adaptation of form in trabecular bone, Nature 405 (6787) (2000) 704–706.

[16] D. Sumner, Long-term implant fixation and stress-shielding in total hip replacement, J. Biomech. 48 (5) (2015) 797–800.

[17] X. Wang, S. Xu, S. Zhou, W. Xu, M. Leary, P. Choong, M. Qian, M. Brandt, Y.M. Xie, Topological design and additive manufacturing of porous metals for bone scaffolds and orthopaedic implants: a review, Biomaterials 83 (2016) 127–141.

[18] S.J.P. Callens, N. Tümer, A.A. Zadpoor, Hyperbolic origami-inspired folding of triply periodic minimal surface structures, Applied, Mater. Today 15 (2019) 453–461.

[19] S.J.P. Callens, D.C.T. né Betts, R. Müller, A.A. Zadpoor, The local and global geometry of trabecular bone, Acta Biomater. 130 (2021) 343–361.

[20] H.M.A. Kolken, A. Zadpoor, Auxetic mechanical metamaterials, RSC Adv. 7 (9) (2017) 5111–5129.

[21] C.P. de Jonge, H. Kolken, A.A. Zadpoor, Non-auxetic mechanical metamaterials, Materials 12 (4) (2019) 635.

[22] K.A. Brakke, The surface evolver, Exp. Math. 1 (2) (1992) 141–165.

[23] K.M. Moerman, GIBBON: the geometry and image-based bioengineering add-on, J. Open Source Softw. 3 (22) (2018) 506.

[24] S. Truscello, G. Kerckhofs, S. Van Bael, G. Pyka, J. Schrooten, H. Van, Oosterwyck, Prediction of permeability of regular scaffolds for skeletal tissue engineering: a combined computational and experimental study, Acta Biomater. 8 (4) (2012) 1648–1658.

[25] I. Standard, Mechanical testing of metals—ductility testing—compression test for porous and cellular metals, ISO 13314: 2011 (E), Ref. Number ISO 13314 (13314) (2011) 1–7.

[26] S. Kalidindi, A. Abusafieh, E. El-Danaf, Accurate characterization of machine compliance for simple compression testing, Exp. Mech. 37 (2) (1997) 210–215.

[27] F. Warmuth, F. Osmanlic, L. Adler, M.A. Lodes, C. Körner, Fabrication and characterisation of a fully auxetic 3D lattice structure via selective electron beam melting, Smart Mater. Struct. 26 (2) (2016), 025013.

[28] G. Dong, Y. Tang, Y.F. Zhao, A 149 line homogenization code for three-dimensional cellular materials written in matlab, J. Eng. Mater. Technol. 141 (1) (2019).

[29] R. Wauthle, B. Vrancken, B. Beynaerts, K. Jorissen, J. Schrooten, J.-P. Kruth, J. Van Humbeeck, Effects of build orientation and heat treatment on the microstructure and mechanical properties of selective laser melted Ti6Al4V lattice structures, Addit. Manuf. 5 (2015) 77–84.

[30] L. Liu, P. Kamm, F. García-Moreno, J. Banhart, D. Pasini, Elastic and failure response of imperfect three-dimensional metallic lattices: the role of geometric defects induced by Selective Laser Melting, J. Mech. Phys. Solids 107 (2017) 160–184.

[31] D. Wang, Y. Yang, R. Liu, D. Xiao, J. Sun, Study on the designing rules and processability of porous structure based on selective laser melting (SLM), J. Mater. Process. Technol. 213 (10) (2013) 1734–1742.

[32] S. Van Bael, G. Kerckhofs, M. Moesen, G. Pyka, J. Schrooten, J.-P. Kruth, Micro-CT-based improvement of geometrical and mechanical controllability of selective laser melted Ti6Al4V porous structures, Mater. Sci. Eng.: A 528 (24) (2011) 7423–7431.

[33] T. Craeghs, S. Clijsters, E. Yasa, F. Bechmann, S. Berumen, J.-P. Kruth, Determination of geometrical factors in Layerwise Laser Melting using optical process monitoring, Opt. Lasers Eng. 49 (12) (2011) 1440–1446.

[34] S.L. Sing, F.E. Wiria, W.Y. Yeong, Selective laser melting of lattice structures: a statistical approach to manufacturability and mechanical behavior, Robot. Comput. -Integr. Manuf. 49 (2018) 170–180.

[35] I. Masters, K. Evans, Models for the elastic deformation of honeycombs, Compos. Struct. 35 (4) (1996) 403–422.

[36] L. Yang, O. Harrysson, H. West, D. Cormier, Mechanical properties of 3D re-entrant honeycomb auxetic structures realized via additive manufacturing, Int. J. Solids Struct. 69 (2015) 475–490.

[37] J.N. Grima, L. Oliveri, D. Attard, B. Ellul, R. Gatt, G. Cicala, G. Recca, Hexagonal honeycombs with zero Poisson's ratios and enhanced stiffness, Adv. Eng. Mater. 12 (9) (2010) 855–862.

[38] C. Li, H. Lei, Z. Zhang, X. Zhang, H. Zhou, P. Wang, D. Fang, Architecture design of periodic truss-lattice cells for additive manufacturing, Addit. Manuf. 34 (2020), 101172.

[39] S. Ren, Y. Chen, T. Liu, X. Qu, Effect of build orientation on mechanical properties and microstructure of Ti-6Al-4V manufactured by selective laser melting, Metall. Mater. Trans. A 50 (9) (2019) 4388–4409.

[40] H. Lei, C. Li, J. Meng, H. Zhou, Y. Liu, X. Zhang, P. Wang, D. Fang, Evaluation of compressive properties of SLM-fabricated multi-layer lattice structures by experimental test and μ-CT-based finite element analysis, Mater. Des. 169 (2019), 107685.

[41] G. Campoli, M. Borleffs, S.A. Yavari, R. Wauthle, H. Weinans, A.A. Zadpoor, Mechanical properties of open-cell metallic biomaterials manufactured using additive manufacturing, Mater. Des. 49 (2013) 957–965.

[42] D. Melancon, Z. Bagheri, R. Johnston, L. Liu, M. Tanzer, D. Pasini, Mechanical characterization of structurally porous biomaterials built via additive manufacturing: experiments, predictive models, and design maps for load-bearing bone replacement implants, Acta Biomater. 63 (2017) 350–368.

[43] T. Wang, L. Wang, Z. Ma, G.M. Hulbert, Elastic analysis of auxetic cellular structure consisting of re-entrant hexagonal cells using a strain-based expansion homogenization method, Mater. Des. 160 (2018) 284–293.

[44] H.M.A. Kolken, K. Lietaert, T. van der Sloten, B. Pouran, A. Meynen, G. Van Loock, H. Weinans, L. Scheys, A.A. Zadpoor, Mechanical performance of auxetic meta-biomaterials, J. Mech. Behav. Biomed. Mater. 104 (2020), 103658.

[45] P.-I. Branemark, Osseointegrated implants in the treatment of the edentulous jaw. Experience from a 10-year period, Scand. J. Plast. Reconstr. Surg. Suppl. 16 (1977) 1–132.

[46] Y. Liu, B. Rath, M. Tingart, J. Eschweiler, Role of implants surface modification in osseointegration: A systematic review, J. Biomed. Mater. Res. Part A 108 (3) (2020) 470–484.

[47] X. Weng, H. Yang, J. Xu, X. Li, Q. Liao, J. Wang, In vivo testing of porous Ti-25Nb alloy serving as a femoral stem prosthesis in a rabbit model, Exp. Ther. Med. 12 (3) (2016) 1323–1330.

[48] V. Karageorgiou, D. Kaplan, Porosity of 3D biomaterial scaffolds and osteogenesis, Biomaterials 26 (27) (2005) 5474–5491.

[49] T. Albrektsson, C. Johansson, Osteoinduction, osteoconduction and osseointegration, Eur. Spine J. 10 (2) (2001) S96–S101.

[50] T. Albrektsson, A. Wennerberg, On osseointegration in relation to implant surfaces, Clin. Implant Dent. Relat. Res. 21 (2019) 4–7.

[51] N. Abbasi, S. Hamlet, R.M. Love, N.-T. Nguyen, Porous scaffolds for bone regeneration, J. Sci. Adv. Mater. Devices 5 (1) (2020) 1–9.

[52] A. Du Plessis, I. Yadroitsava, I. Yadroitsev, S. Le Roux, D. Blaine, Numerical comparison of lattice unit cell designs for medical implants by additive manufacturing, Virtual Phys. Prototyp. 13 (4) (2018) 266–281.

[53] H.-S. Han, S. Loffredo, I. Jun, J. Edwards, Y.-C. Kim, H.-K. Seok, F. Witte, D. Mantovani, S. Glyn-Jones, Current status and outlook on the clinical translation of biodegradable metals, Mater. Today 23 (2019) 57–71.

[54] Y. Li, J. Zhou, P. Pavanram, M. Leeflang, L. Fockaert, B. Pouran, N. Tümer, K.-U. Schröder, J. Mol, H. Weinans, Additively manufactured biodegradable porous magnesium, Acta Biomater. 67 (2018) 378–392.

[55] Y. Li, H. Jahr, K. Lietaert, P. Pavanram, A. Yilmaz, L. Fockaert, M. Leeflang, B. Pouran, Y. Gonzalez-Garcia, H. Weinans, Additively manufactured biodegradable porous iron, Acta Biomater. 77 (2018) 380–393.

[56] Y. Li, P. Pavanram, J. Zhou, K. Lietaert, P. Taheri, W. Li, H. San, M. Leeflang, J. Mol, H. Jahr, Additively manufactured biodegradable porous zinc, Acta Biomater. 101 (2020) 609–623.

[57] Y. Li, H. Jahr, P. Pavanram, F. Bobbert, U. Puggi, X.-Y. Zhang, B. Pouran, M. Leeflang, H. Weinans, J. Zhou, Additively manufactured functionally graded biodegradable porous iron, Acta Biomater. 96 (2019) 646–661.